

# An Exhaustive Symmetry Approach to Structure Determination: Phase Transitions in $\text{Bi}_2\text{Sn}_2\text{O}_7$

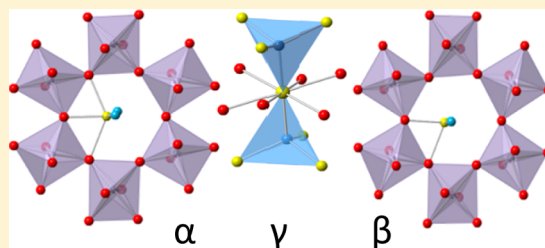
James W. Lewis,<sup>†</sup> Julia L. Payne,<sup>†</sup> Ivana Radosavljevic Evans,<sup>†</sup> Harold T. Stokes,<sup>‡</sup> Branton J. Campbell,<sup>‡</sup> and John S. O. Evans<sup>\*,†</sup>

<sup>†</sup>Department of Chemistry, University Science Site, Durham University, South Road, Durham DH1 3LE, United Kingdom

<sup>‡</sup>Department of Physics & Astronomy, Brigham Young University, Provo, Utah 84602, United States

## S Supporting Information

**ABSTRACT:** The exploitable properties of many materials are intimately linked to symmetry-lowering structural phase transitions. We present an automated and exhaustive symmetry-mode method for systematically exploring and solving such structures which will be widely applicable to a range of functional materials. We exemplify the method with an investigation of the  $\text{Bi}_2\text{Sn}_2\text{O}_7$  pyrochlore, which has been shown to undergo transitions from a parent  $\gamma$  cubic phase to  $\beta$  and  $\alpha$  structures on cooling. The results include the first reliable structural model for  $\beta$ - $\text{Bi}_2\text{Sn}_2\text{O}_7$  (orthorhombic  $Aba2$ ,  $a = 7.571833(8)$ ,  $b = 21.41262(2)$ , and  $c = 15.132459(14)$  Å) and a much simpler description of  $\alpha$ - $\text{Bi}_2\text{Sn}_2\text{O}_7$  (monoclinic  $Cc$ ,  $a = 13.15493(6)$ ,  $b = 7.54118(4)$ , and  $c = 15.07672(7)$  Å,  $\beta = 125.0120(3)^\circ$ ) than has been presented previously. We use the symmetry-mode basis to describe the phase transition in terms of coupled rotations of the  $\text{Bi}_2\text{O}'$  anti-cristobalite framework, which allow Bi atoms to adopt low-symmetry coordination environments favored by lone-pair cations.



## INTRODUCTION

Many functional materials have exploitable properties that are intimately associated with symmetry-lowering phase transitions induced as a function of an external variable such as temperature, pressure, or chemical composition. Typical examples include materials showing one of the ferroic orders (ferroelectric, ferromagnetic, and ferroelastic), second harmonic generation (SHG) switches, positive-to-negative thermal expansion changes, and structurally induced insulator to metal/superconductor transitions.<sup>1–8</sup> Such transitions can lead to complex superstructures which can be difficult to determine using conventional characterization approaches, particularly when only polycrystalline samples are available. Here we describe an exhaustive approach using symmetry-adapted distortion modes (which we refer to as “symmetry modes”) and automatically generated group–subgroup trees which we believe will be widely applicable to such problems. We demonstrate the approach on pyrochlore-type  $\text{Bi}_2\text{Sn}_2\text{O}_7$ , the structural chemistry of which has been the subject of considerable debate. Our approach allows us to systematically determine and describe what we believe are definitive structural models for the  $\alpha$ -,  $\beta$ -, and  $\gamma$ -phases, and resolve their conflicting descriptions in the literature.

Pyrochlore structures have been widely studied due to the range of important properties they exhibit, including ferroelectricity,<sup>9</sup> dielectric properties,<sup>10</sup> superconductivity,<sup>11</sup> oxide-ion conductivity,<sup>12</sup> colossal magnetoresistance (CMR),<sup>13</sup> CO sensing,<sup>14</sup> metal–semiconductor transitions,<sup>15</sup> spin-ice magnetic frustration,<sup>16</sup> radio-isotope isolation,<sup>17</sup> and photocatalysis.<sup>18</sup> Materials with the ideal pyrochlore structure crystallize in

space group  $Fd\bar{3}m$  and have general formula  $A_2B_2O_6O'$  (Figure 1). With origin choice 2, A cations (generally 2+ or 3+) occupy 16c positions, B cations (generally 4+ or 5+) occupy 16d positions, O anions occupy 48f sites, and  $O'$  anions occupy 8a sites. There is a single freely refineable atomic coordinate: the  $x$  coordinate of O. It is often helpful to think of the pyrochlore structure as interpenetrating  $A_2O'$  and  $B_2O_6$  frameworks.<sup>19</sup> The  $A_2O'$  framework contains corner-sharing  $A_{4/2}O'$  tetrahedra with the anti-cristobalite arrangement, and the  $B_2O_6$  framework contains corner-sharing  $BO_{6/2}$  octahedra. The interpenetration of the two frameworks leads to A cations having a distorted hexagonal bipyramidal coordination environment:  $AO_6O'_2$ , typically with six longer equatorial bonds arranged in a puckered hexagon and shorter axial bonds.

There has been significant interest in pyrochlores with Bi(III) on the A site, where the stereochemically active Bi lone pair leads to it moving away from its high-symmetry coordination environment. In  $\text{Bi}_2\text{Ti}_2\text{O}_7$ , first synthesized and characterized by Radosavljevic et al.,<sup>20</sup> Rietveld refinement suggests Bi displacement to 96h sites (toward a hexagon edge) rather than to 96g sites (directly toward an oxygen or hexagon corner). Subsequent Pair Distribution Function (PDF) studies also concluded that Bi positions are preferentially displaced to 96h, with short-range correlations of  $\text{Bi}_4\text{O}$  tetrahedral displacements.<sup>21,22</sup> The frustration of long-range coherent off-center displacements of Bi was discussed by Seshadri as being responsible for preventing a paraelectric-to-ferroelectric phase

Received: May 13, 2016

Published: June 1, 2016

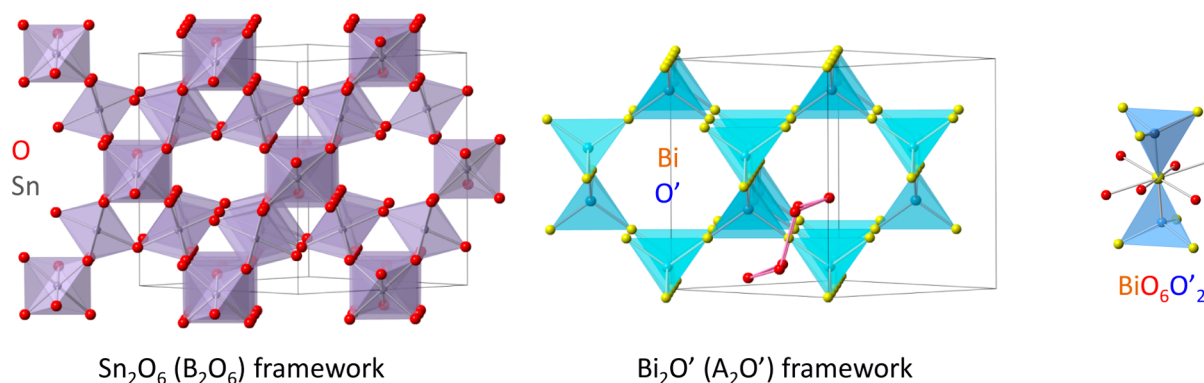


**Figure 1.** Pyrochlore structure of  $\text{Bi}_2\text{Sn}_2\text{O}_7$  ( $\text{Bi}_2\text{Sn}_2\text{O}_6\text{O}'$ ) emphasizing (left) the corner-sharing  $\text{SnO}_{6/2}$  octahedral framework and (center) the interpenetrating  $\text{Bi}_{4/2}\text{O}'$  anti-cristobalite framework. Right-most view shows one puckered hexagonal  $\text{O}_6$  ring that completes the  $\text{BiO}_6\text{O}'_2$  coordination environment of each Bi.

transition.<sup>23</sup> The term “charge ice” has been coined in analogy to the “spin ice” properties of materials such as  $\text{Dy}_2\text{Ti}_2\text{O}_7$ <sup>16</sup> and  $\text{Ho}_2\text{Ti}_2\text{O}_7$ .<sup>24,25</sup> Other examples include the electrocatalyst  $\text{Bi}_2\text{Ru}_2\text{O}_6\text{O}'_{1-\beta}$ ,<sup>26</sup> where simulation of diffuse scattering in electron-diffraction data points to distributions of Bi positions in a disc similar to that observed for  $\text{Bi}_2\text{Ti}_2\text{O}_6\text{O}'$ .<sup>27</sup> Wang et al. have discussed the influence of B-site covalency on Bi distortions in pyrochlore bismuth zinc niobates and suggested that more-ionic B sites (e.g., Sn, Ti) are more likely to distort from cubic symmetry.<sup>28</sup> Local bonding requirements, distortions, and cation order are also known to be important in controlling dielectric properties of materials such as  $\text{Bi}_2(\text{Zn}_{1/3}\text{Nb}_{2/3})_2\text{O}_7$ .<sup>29–31</sup>

$\text{Bi}_2\text{Sn}_2\text{O}_7$  has shown potential for technological applications in catalytic oxidation of isobutene,<sup>32–34</sup> methane coupling,<sup>35</sup> photocatalysis,<sup>36</sup> and selective carbon monoxide sensing.<sup>14,37–39</sup> It was first reported by Roth<sup>40</sup> in 1956 as having a diffraction pattern similar to that of cubic pyrochlores but with additional peaks pointing to a distorted structure. The first report of polymorphism in  $\text{Bi}_2\text{Sn}_2\text{O}_7$  was given by Shannon and co-workers.<sup>41</sup> They described three pyrochlore-related forms: a high-temperature (>900 K)  $\gamma$ -phase, an intermediate-temperature (390–900 K)  $\beta$ -phase, and a low-temperature  $\alpha$ -phase, all with pyrochlore-related structures. The transition from  $\gamma$  to  $\beta$  was reported as second order, and both the  $\alpha$ - and  $\beta$ -phases were SHG active. The high-temperature  $\gamma$ -form is relatively uncontroversial. Its average structure is that of a cubic pyrochlore with  $a_{\text{cub}} = 10.73$  Å, though with local distortions due to Bi(III) ions moving off the ideal pyrochlore site.<sup>20,42–44</sup>

The intermediate  $\beta$ - $\text{Bi}_2\text{Sn}_2\text{O}_7$  was reported as being face-centered-cubic with  $a = 21.4$  Å ( $2a_{\text{cub}}$ ), and room-temperature  $\alpha$ - $\text{Bi}_2\text{Sn}_2\text{O}_7$  as body-centered tetragonal with  $a = b = 15.14$  Å and  $c = 21.4$  Å ( $\sqrt{2}a_{\text{cub}}$ ,  $\sqrt{2}a_{\text{cub}}$ ,  $2a_{\text{cub}}$ ).<sup>41</sup> Despite attempts by several groups, no reliable structures for  $\alpha$ - or  $\beta$ - $\text{Bi}_2\text{Sn}_2\text{O}_7$  were reported until Evans et al.<sup>45</sup> performed an exhaustive study of the 21 different structures possible for  $\alpha$ - $\text{Bi}_2\text{Sn}_2\text{O}_7$  based on three assumptions: that  $\alpha$ ,  $\beta$ , and  $\gamma$  follow group–subgroup relationships; that  $\beta$  has a yet-unknown and apparently cubic structure with a cell edge of  $2a_{\text{cub}}$ ; and that  $\alpha$  and  $\beta$  are SHG active. They concluded that, under these assumptions, the diffraction data of  $\alpha$ - $\text{Bi}_2\text{Sn}_2\text{O}_7$  could only be accurately described using a monoclinic  $Pc$  structure with 176 crystallographically unique atoms. For clarity we refer to this model as  $\alpha_{\text{old}}\text{-Bi}_2\text{Sn}_2\text{O}_7$  throughout this paper. New experimental studies on  $\beta$ - $\text{Bi}_2\text{Sn}_2\text{O}_7$  by us and others<sup>46,47</sup> have revealed additional

weak reflections and peak splittings inconsistent with a face-centered cubic cell, indicating lower symmetry. Salamat et al.<sup>47</sup> proposed a  $\beta$ - $\text{Bi}_2\text{Sn}_2\text{O}_7$  model in space group  $P3_1$  with cell parameters of  $a = 7.55$  ( $a_{\text{cub}}/\sqrt{2}$ ) and  $c = 37.01$  Å ( $2\sqrt{3}a_{\text{cub}}$ ) which was metrically cubic and has a cell volume of  $1.5 \times V_{\text{cub}}$ . However, this model does not fit high-resolution powder diffraction data from the  $\beta$ -phase and shows no obvious symmetry relationship to the  $\alpha_{\text{old}}$  or  $\gamma$  forms, suggesting that it needs revisiting.

The new experimental observations on  $\beta$ - $\text{Bi}_2\text{Sn}_2\text{O}_7$  clearly invalidate some of the assumptions used to determine the  $\alpha_{\text{old}}$  model of  $\alpha$ - $\text{Bi}_2\text{Sn}_2\text{O}_7$ . This, and insight from the symmetry-mode analysis discussed below, has prompted us to also revisit the structural chemistry of both  $\alpha$ - and  $\beta$ - $\text{Bi}_2\text{Sn}_2\text{O}_7$ . To allow a systematic exploration of all the possible structures for the  $\alpha$ - and  $\beta$ -phases, we report an automated exhaustive approach for producing candidate models, generating their symmetry-mode parameterizations, and performing combined symmetry-mode refinements against X-ray and neutron diffraction data sets. This approach allows us to identify a simpler structural description for  $\alpha$ - $\text{Bi}_2\text{Sn}_2\text{O}_7$  and a new structural model for  $\beta$ - $\text{Bi}_2\text{Sn}_2\text{O}_7$ . We describe the important local structural distortions in each phase and the structural relationships between them.

The method we report allows a systematic and exhaustive search of the structural landscape accessible following a symmetry-changing phase transition. We therefore believe that the approach is broadly applicable and will be of significant importance in the study of a wide range of functional materials.

## ■ EXPERIMENTAL SECTION

$\text{Bi}_2\text{Sn}_2\text{O}_7$  was prepared from stoichiometric quantities of  $\text{Bi}_2\text{O}_3$  (1.214 g, 2.61 mmol) and  $\text{SnO}_2$  (0.786 g, 5.22 mmol) which were intimately ground in a mortar and pestle and fired at 1373 K for 16 h. Powder diffraction indicated formation of a single-phase product. The sample was reheated to 1223 K immediately prior to synchrotron and neutron powder diffraction experiments. Synchrotron X-ray data were collected at the Diamond I11 beamline on a sample loaded in a 0.3 mm capillary from  $2^\circ$  to  $140^\circ$  for 2 h at 293 K and 4 h at 470 K using a wavelength of 0.82644 Å and high-resolution multi-analyzer crystal (MAC) detectors. Rapid data collections were performed from 250 to 470 K using a data collection time of 2 min per scan. Neutron diffraction data were collected on the high-resolution powder diffractometer HRPD at ISIS over a time-of-flight range of 30–130 ms at 298 and 473 K with total data collection times of 8 h (250  $\mu\text{Ah}$ ).

To undertake the structural work reported in this paper, a new feature was added to the ISODISTORT software package<sup>48</sup> which outputs an exhaustive listing of the intermediate structures that fall

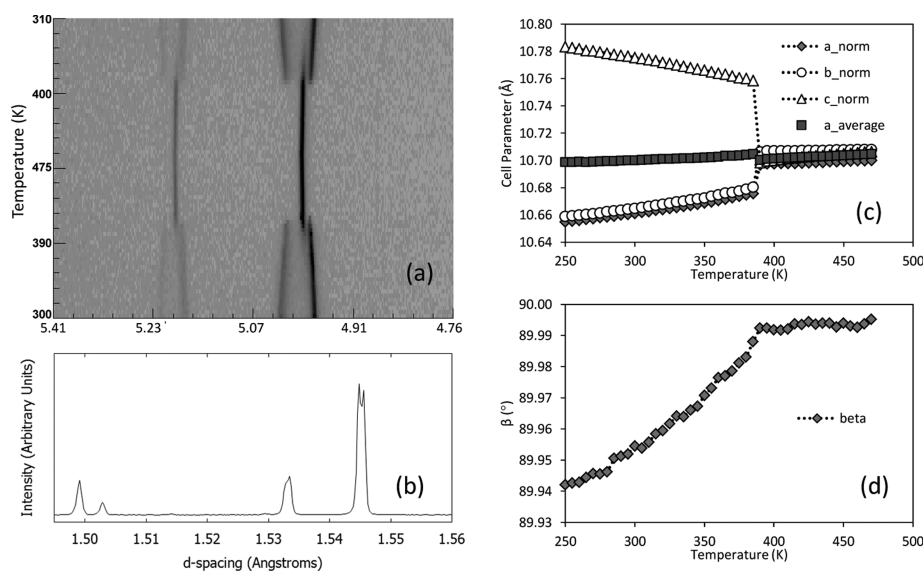


**Figure 2.** 2D image of Synchrotron X-ray data showing (a) the  $\alpha$ - to  $\beta$ -phase transition on heating, then the  $\beta$ - to  $\alpha$ -phase transition on cooling, (b) peak splitting in the  $\beta$ -phase, and (c,d) cell parameters derived using the  $\alpha_{old}$  model from cooling data and normalized to the cubic  $\gamma$ -cell.

between a parent structure and a distorted child structure, i.e., the structures whose symmetry groups are intermediate to the parent and child symmetry groups. Multiple domains of a given subgroup are treated as duplicates, so that only one domain of each subgroup is listed in the tree. In addition to a variety of useful descriptive information (e.g., space group, sublattice basis and origin, cell parameters, symmetry index, etc.), ISODISTORT automatically generates a symmetry-mode parameterization of each structure from the subgroup tree in TOPAS .str format, and bundles them all into a single downloadable zip file. We note that the new SUBGROUP program of the Bilbao Crystallographic Server also generates trees of intermediate subgroups,<sup>49–51</sup> though the nature of its output is somewhat different. Preliminary comparisons of ISODISTORT and SUBGROUP showed their subgroup calculations to be mutually consistent.

These routines were used to generate an exhaustive listing of the intermediate structures that fall between the parent  $\gamma$ -structure and a child structure of sufficiently low symmetry to include all structural parameters relevant to either the  $\alpha$ - or  $\beta$ -phase of  $\text{Bi}_2\text{Sn}_2\text{O}_7$ .

Investigation of each of the candidate models in the subgroup tree was automated using Python 2.7 routines to control Rietveld refinements performed using the Topas Academic software.<sup>52,53</sup> For each structure in the tree, a command file for combined symmetry-mode Rietveld refinement against X-ray and neutron data was produced automatically from a template in the TOPAS .inp format. The best Rietveld fit was then determined by a process of repeated local minimization (RLM) from random starting values. Experimental peak shapes, instrument calibration constants, and the background description were fixed during this process. To improve speed, we used a  $q$  range corresponding to  $d_{min} = 1.2$  Å; tests showed that this range was sufficient to distinguish distinct candidate models. Owing to the complexity of some of the structural models (a child  $P1$  description of  $\alpha_{old}\text{-Bi}_2\text{Sn}_2\text{O}_7$  has 1056 displacive structural degrees of freedom, 6 cell parameters, and 2 scale factors, making Rietveld refinement relatively slow), we found it convenient to partially separate the determination of cell parameters and mode amplitudes. For each candidate model, 5000 rapid least-squares iterations were initially performed with mode amplitudes fixed at zero and only symmetry-constrained cell parameters refining. After each convergence, the variable cell parameters were randomized by  $\pm 1\%$  and refined back to convergence. In a second cycle, a further 2000 least-squares iterations were performed with cell parameters randomized by  $\pm 0.1\%$  around these predetermined values and all mode amplitudes allowed to vary. To help convergence, we applied a weak restraint to keep non-important mode amplitudes close to zero. After each convergence,

mode amplitudes were reset to random values between  $-0.1$  and  $+0.1$ . Key output parameters were automatically collated by the Python routines. Using this procedure on a modest desktop PC (i7, 3.4 GHz), we could analyze the 547 candidate models contained in the subgroup tree in around 48 h. Several repeat runs were performed and  $R_{wp}$  differences of  $<0.1\%$  were typically found for a given candidate model between different runs (see Supporting Information (SI) Figure S1). We also found that obvious subgroups of a given candidate model always gave an essentially equivalent or lower  $R_{wp}$ . These observations suggest that we successfully found the lowest  $R_{wp}$  fit to the data for each candidate model.

For final Rietveld refinements used to extract detailed structural information, X-ray and neutron data were simultaneously fitted to  $d_{min} = 0.7$  Å. Instrumental contributions to peak shapes and the X-ray wavelength were determined from  $\text{LaB}_6$  and  $\text{Si/CeO}_2$  standards for synchrotron and neutron data, respectively. Absorption corrections were refined using room-temperature data. For the  $\beta$ -phase we refined a total of 64 mode amplitudes, 3 cell parameters, and 4 isotropic temperature factors (equating Bi-, Sn-, O-, and O'-derived sites of the parent) for the 24 symmetry-independent atoms, though one  $\Gamma_4$  mode was set at zero to fix the origin. An additional 50 parameters were used to describe background, peak shape and other experimental effects. For the  $\alpha$ -phase, 66 mode amplitudes (22 unique atoms) were refined, two of which fixed the origin. The  $\alpha$ -phase peaks are significantly broader than those of the  $\beta$ -phase and also show a slight  $hkl$ -dependent width and asymmetry (see Figure 6 and SI Figure S2). We therefore introduced a Stephens-type strain broadening for final refinements giving  $R_{wp} = 5.6\%$ .<sup>54</sup> Strain broadening is unsurprising given the significant cell-metric change ( $\Delta d/d \approx 1 \times 10^{-2}$ ) which occurs at the first-order  $\beta$ - to  $\alpha$ -phase transition at 390 K. An excellent fit reproducing the observed asymmetry can also be achieved using a multi-phase model where the cell parameters and phase fractions of a set of structurally identical phases are parameterized to describe the strain broadening. Only six parameters are required in this approach, and a lower  $R_{wp}$  is obtained than with the Stephens approach (4.9%) (SI Figure S2). Both models result in essentially identical refined-mode amplitudes. Effective polyhedral tilt angles in each final structure were determined using GASP.<sup>55,56</sup>

## RESULTS AND DISCUSSION

**Variable-Temperature Diffraction Data and the  $\alpha_{old}\text{-Bi}_2\text{Sn}_2\text{O}_7$  Model.** High-resolution synchrotron X-ray and neutron ( $\Delta d/d \approx 10^{-4}$  Å) powder diffraction data were collected up to 473 K on  $\text{Bi}_2\text{Sn}_2\text{O}_7$ . Despite being derived from

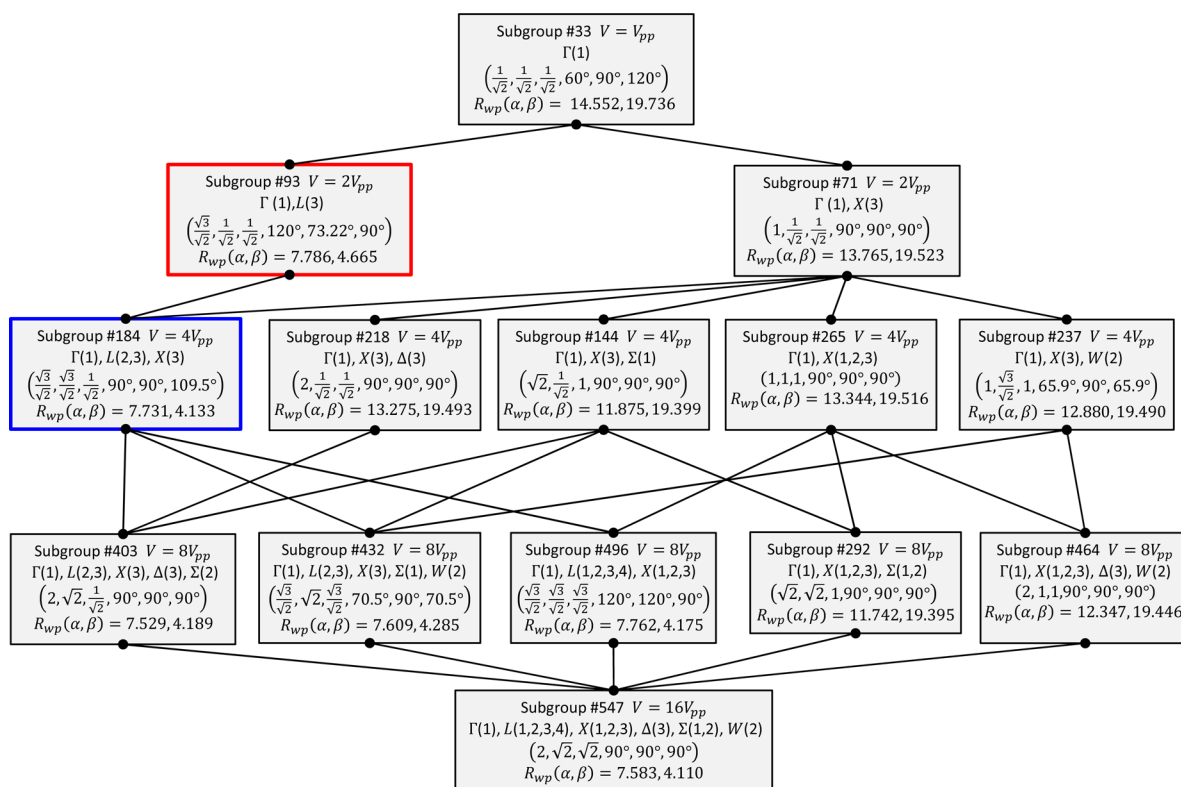


**Figure 3.** Lattice–sublattice relationships among the 14 lattice subgroups extracted from the tree of 547 intermediate subgroups. For each entry, the first line shows the subgroup candidate number and the cell volume (relative to that of the primitive parent cell,  $V_{pp} = 224 \text{ \AA}^3$ ); the second line indicates the active k-vectors; the third line shows the unit cell parameters ( $a/a_{cp}$ ,  $b/a_{cp}$ ,  $c/a_{cp}$ ,  $\alpha$ ,  $\beta$ ,  $\gamma$ ), with edge lengths presented relative to the cubic parent ( $a_{cp} = 10.72 \text{ \AA}$ ) and angles in degrees. A given lattice is linked to each of its minimal superlattices and maximal sublattices with a solid black line. Active k-vectors are numbered corresponding to their positions in Table 1. For example, the set of active k-vectors of lattice subgroup #184 includes the only arm of the star of GM, the second and third of four arms of the star of L, and the third of three arms of the star of X. At minimum, the set of active k-vectors of a given lattice must contain all of the active k-vectors of each of its maximal superlattices, though it will generally contain other k-vectors too. The lattice subgroups found for  $\alpha$ - and  $\beta$ - $\text{Bi}_2\text{Sn}_2\text{O}_7$  are shown in red and blue boxes, respectively.

medium resolution powder data ( $\Delta d/d \approx 10^{-2}$  Å), the published  $Pc$   $\alpha_{old}$ - $\text{Bi}_2\text{Sn}_2\text{O}_7$  structure gave an essentially flawless fit to room-temperature high-resolution data without refining any structural parameters. Refinement of the model against variable-temperature diffraction data gave clear evidence for the first-order phase transition to  $\beta$ - $\text{Bi}_2\text{Sn}_2\text{O}_7$  at 390 K (Figure 2). The monoclinic cell angle freely refined to  $89.995(1)^\circ$  (i.e.,  $90^\circ$  to the true precision of the experiment) for the  $\beta$ -phase. From neutron data the  $\beta$  cell appears metrically cubic, but the higher resolution X-ray data reveal small peak splittings, suggesting lower metric symmetry (Figure 2b). The idea that the  $\alpha$ -phase structure descends in symmetry from a face-centered-cubic  $\beta$ -phase structure was a key literature-based assumption in the 2003 derivation of the  $\alpha_{old}$  model of  $\alpha$ - $\text{Bi}_2\text{Sn}_2\text{O}_7$ , which is therefore incorrect.

In addition, our  $\beta$ -phase diffraction data show weak superstructure reflections at the X point in reciprocal space, which are not present in the  $\alpha$  data. It is interesting that these superlattice reflections can be adequately fitted when the  $\alpha_{old}$ - $\text{Bi}_2\text{Sn}_2\text{O}_7$  model is refined against the  $\sim 473$  K  $\beta$ -phase data, but have zero calculated and observed intensity when it is refined against  $\alpha$ -phase data at room temperature (Figure S3). These observations suggest that a simpler model may be possible for  $\alpha$ - $\text{Bi}_2\text{Sn}_2\text{O}_7$ , and that the  $\alpha_{old}$  model may actually be a common isotropy subgroup of both the correct  $\alpha$ - and  $\beta$ -phase structures.

### Lattices of the $\beta$ - and $\alpha$ - $\text{Bi}_2\text{Sn}_2\text{O}_7$ Superstructures.

Experimentally, we observe that all the clearly separable superlattice peaks in the powder diffraction data of either the  $\alpha$ - or  $\beta$ -phases are associated with the L or X points in reciprocal space (see Figure S3). Assuming that we have not missed any points, we can superpose the most general L- and X-point order-parameter directions to obtain a  $P1$  symmetry superstructure with cell parameters of  $a \approx b \approx c \approx \sqrt{2}a_{cub} \approx 15.16 \text{ \AA}$ ,  $\alpha \approx \beta \approx 120^\circ$ ,  $\gamma \approx 90^\circ$ , and  $V \approx 2V_{cub}$ . The superstructure must have sufficient degrees of freedom to capture any structural features of either the  $\alpha$ - or  $\beta$ -phases. For this work, we further opted to double the cell volume according to  $a = b = 15.14 \text{ \AA}$ ,  $c = 21.4 \text{ \AA}$ ,  $\alpha \approx \beta \approx \gamma \approx 90^\circ$ , and  $V \approx 4V_{cub}$ , in order to keep the larger  $\alpha_{old}$ - $\text{Bi}_2\text{Sn}_2\text{O}_7$  model within the scope of our analysis. The primary hypothesis in our present exploration of possible superstructures for  $\alpha$ - and  $\beta$ - $\text{Bi}_2\text{Sn}_2\text{O}_7$  is that their isotropy subgroups must be supergroups of this “base” structure and subgroups of the “parent”  $\gamma$ -phase structure. The collection of all such candidates comprise a “tree” of intermediate subgroups.

A newly released subgroup tree feature in ISODISTORT was used to generate an exhaustive list of distinct intermediate subgroups that are both subgroups of the parent  $\gamma$ -phase symmetry and supergroups of the base  $P1$  subgroup. A total of 547 distinct candidate subgroups are predicted, each with a corresponding refinable structural model. Of these, two are incapable of supporting atomic displacements beyond those of

Table 1. Top: The 14 Lattice Subgroups and Their Fit to Both  $\beta$ - and  $\alpha$ -Phase Data;<sup>a</sup> Bottom: Arms of the Star of the k-Vector for Each Type of Reciprocal-Space k-Vector<sup>b</sup>

Subgroup #	$\beta$ Rank	$\beta$ Rwp (%)	$\alpha$ Rank	$\alpha$ Rwp (%)	$V_{\text{frac}}$	#Prms	$\Gamma$	$L$	$X$	$\Delta$	$\Sigma$	$W$	min superlattices	max sublattices	
547	1	4.110	1	7.543	4.00	1056	1	1,2,3,4	1,2,3	3	1,2	2	292, 403, 432, 464, 496	none	
184	2	4.133	10	7.729	1.00	264	1	2,3	3				93	403, 432, 496	
496	3	4.175	11	7.794	2.00	528	1	1,2,3,4	1,2,3				184, 265	547	
403	8	4.189	2	7.545	2.00	528	1	2,3	3	3	2		184, 218, 144	547	
432	22	4.285	6	7.596	2.00	528	1	2,3	3		1	2	184, 144, 237	547	
93	30	4.665	15	7.849	0.50	132	1	3					33	184	
292	286	19.395	221	12.578	2.00	528	1		1,2,3		1,2		144, 265	547	
144	287	19.399	225	12.758	1.00	264	1		3		1		71	403, 432, 292	
464	288	19.446	215	12.347	2.00	528	1		1,2,3	3		2	237, 265	547	
237	294	19.490	231	12.880	1.00	264	1		3			2	71	432, 464	
218	296	19.493	255	13.404	1.00	264	1		3	3			71	403	
265	299	19.516	257	13.440	1.00	264	1		1,2,3				71	292, 464, 496	
71	304	19.523	279	13.840	0.50	132	1		3				33	144, 218, 237, 265	
33	355	19.736	316	14.619	0.25	66	1						none	71, 93	
k-point	1	2	3	4	5	6									
$\Gamma$ :	(0,0,0)														
$L$ :	(1/2,1/2,1/2)	(-1/2,1/2,1/2)	(1/2,-1/2,1/2)	(1/2,1/2,-1/2)											
$X$ :	(0,1,0)	(1,0,0)	(0,0,1)												
$\Delta$ :	(0,1/2,0)	(1/2,0,0)	(0,0,1/2)												
$\Sigma$ :	(1/2,1/2,0)	(1/2,-1/2,0)	(1/2,0,1/2)	(1/2,0,-1/2)	(0,1/2,1/2)	(0,1/2,-1/2)									
$W$ :	(1/2,1,0)	(1,0,1/2)	(0,1/2,1)												

<sup>a</sup>Candidate models are listed in the rank order of their  $R_{\text{wp}}$  fit to  $\beta$ -data. The active arms of the star of each k-vector are denoted numerically in reference to the possible arms. <sup>b</sup>For each type of reciprocal-space k-vector that contributes to the sublattices of one or more of the 547 intermediate subgroups, we list the arms of the star of the k-vector (or rather the combined star of  $\pm k$ ). The active k-vectors of any candidate model must come from this list. Lattice subgroups above the red and blue lines have sufficient active k-points to fit the  $\alpha$ - and  $\beta$ -phase data respectively.

the parent structure, and therefore receive no more attention. The full tree is listed in the SI (Table S1) according to their candidate number (#).

To help restrict the choice of candidate models, it was useful to separately consider the smaller tree of 14 intermediate direct-space lattices that are both sublattices of the face-centered parent  $\gamma$ -phase lattice and superlattices of the primitive base lattice (Figure 3), including the base and parent lattices themselves. We refer to this set of 14  $P1$  subgroups as “lattice subgroups”. Every candidate model in the 547-member tree is associated with exactly one of these 14 lattice subgroups. Because a lattice subgroup combines all of the structural variables of all of the candidate models associated with it, a model based on the lattice subgroup will fit the observed diffraction data at least as well as any of the associated candidate models.

The correct lattice subgroups for  $\alpha$ - and  $\beta$ - $\text{Bi}_2\text{Sn}_2\text{O}_7$  were identified by testing all 14 of them against diffraction data from both phases using the RLM Rietveld approach described in the Experimental Section.  $R_{\text{wp}}$  values for each of these joint neutron/X-ray fits are included in Table 1, which is ordered according to how well candidates fit the  $\beta$ -phase data. Table 1 also lists the active k-vectors for each subgroup. For  $\beta$ - $\text{Bi}_2\text{Sn}_2\text{O}_7$  we see a clear break in  $R_{\text{wp}}$ , from  $>19\%$  to  $\leq 4.7\%$ , for lattice subgroups that possess  $L$ -point modes, and a second smaller but significant break from  $\sim 4.7\%$  to  $\leq 4.3\%$  when  $X$ -point modes become available (the first 5 rows of Table 1, above the blue line). We see that lattice subgroup #184 provides an excellent fit to the data, has a relatively low parameter count (264), and excludes contributions from reciprocal-space points for which we see no evidence of superlattice reflections (i.e.,  $\Delta$ ,  $\Sigma$ ,  $W$ ). It is the clear choice for the primitive lattice of the  $\beta$ -phase. Because the candidate models associated with a given lattice subgroup appear contiguously in ISODISTORT’s subgroup-tree listing (SI Table S1), we can now isolate the

$\beta$ -phase subgroup to lie somewhere on or between candidates #145 and #184 in our tree.

For the  $\alpha$ -phase, each of the lattice subgroups in the first six rows of Table 1 (above the red line) give an excellent fit to the diffraction data, demonstrating that only  $L$ -point modes contribute to the structure, consistent with visual inspections of the clearly separable superlattice reflections. Following the same arguments used for  $\beta$ , we see that lattice subgroup #93 is the clear choice for the  $\alpha$ -phase. The other lattices that lie above the red line in Table 1 are sublattices of #93; we judge that their fits are slightly better only because of their greater parameter counts (see below). The correct  $\alpha$ -phase subgroup must then lie on or between candidates #72 and #93 in our tree. We note that the  $\beta$ -phase lattice (#184) is a maximal sublattice of the primitive  $\alpha$ -phase lattice (#93), and has double the primitive cell volume.

**Exhaustive Subgroup Search.** For the  $\beta$ - and  $\alpha$ -phases, identification of the lattice subgroup restricts the number of candidate models that need to be tested to 40 and 22 respectively. However, in this section we choose to test all 547 candidate models. We do this for three reasons: completeness in this proof-of-concept study; because for this example, it is not much more computationally demanding than testing just the  $P1$  sublattices and the relevant associated candidate models; and because it gives (Figures 4 and 5) a full view of the  $R_{\text{wp}}$  landscape of all possible structures.

We will start by considering the  $\beta$ -phase. The lowest  $R_{\text{wp}}$  values obtained by Rietveld fitting each of the 547 candidates to the  $\beta$ -phase data are shown in Figure 4; corresponding plots for  $\alpha$  are in Figure 5. Figure 4a shows the minimum  $R_{\text{wp}}$  value obtained for each of the 547 candidates ordered by their candidate number in the tree. The general trend is a lowering of  $R_{\text{wp}}$  as symmetry is lowered among subgroups of the same lattice, followed by a sharp increase upon reaching the first (high-symmetry) subgroup of the next lattice.

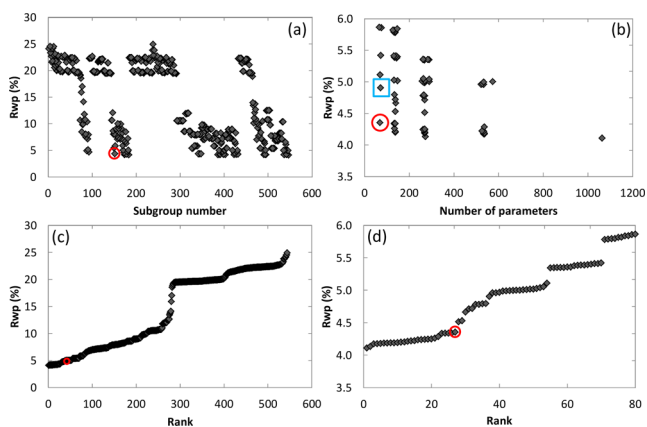


**Figure 4.** Final  $R_{wp}$  values from refinements of the 547 candidate models for  $\beta$ - $\text{Bi}_2\text{Sn}_2\text{O}_7$  against  $\sim 473$  K X-ray and neutron diffraction data. Individual panels show (a) all  $R_{wp}$  values as a function of child candidate number in the tree, (b)  $R_{wp}$  as a function of the number of refined parameters for the 80 lowest- $R_{wp}$  candidates, (c)  $R_{wp}$  values for all candidates in ranked order, and (d) the 80 lowest- $R_{wp}$  candidates in ranked order. “Best” candidates lie toward the bottom left-hand corner of panel b. Candidate #152 (our best  $\beta$ -structure model) is marked with a red circle, and candidate #88 (our best  $\alpha$ -structure model) is marked with a blue square.

Figure 4b plots  $R_{wp}$  as a function of the number of refined parameters (mode amplitudes, cells, and scale factors) for the best 80 candidates. Figure 4c,d plots ranked  $R_{wp}$  values for all candidates and for the best 80 candidates, respectively. From Figure 4a, the candidates can be divided into two broad categories: those with  $R_{wp} \gtrsim 15\%$ , and those with  $R_{wp} \lesssim 15\%$ . As in the lattice subgroup search, the distinction between the two categories is the presence of symmetry modes of the  $L$  point in reciprocal space in the low  $R_{wp}$  candidates. Figure 4b,d shows that there are a number of candidates with  $R_{wp} < 4.5\%$ , all of which give an excellent visual fit to the experimental data. In Figure 4d, the decrease in  $R_{wp}$  at the 27th-ranked candidate (red circle) differentiates models that contain a minimum of essential  $\Gamma$ -,  $X$ -, and  $L$ -point modes from those that do not; candidates above this point lack at least one. Figure 4b shows an expected correlation between the number of structural degrees of freedom in a candidate model and the lowest  $R_{wp}$  achievable. The “good” candidates cluster into those with  $\sim 69$ ,  $\sim 138$ ,  $\sim 272$ ,  $\sim 536$ , and  $\sim 1064$  parameters. The gradual reduction in minimum  $R_{wp}$  with increasing parameter count (from 4.35 to 4.11%) is due to the fact that lowering the symmetry below what is necessary allows a candidate model to falsely compensate for minor discrepancies in peak shapes and intensities. From Figure 4b the stand-out  $\beta$ -phase candidate is therefore #152, which is circled red in each panel. It has 69 parameters,  $R_{wp} = 4.35\%$ , orthorhombic space group  $Aba2$ , and cell metrics of  $a = 7.58 \text{ \AA}$ ,  $b = 21.45 \text{ \AA}$ ,  $c = 15.16 \text{ \AA}$  ( $a_{\text{cub}}/\sqrt{2}$ ,  $2a_{\text{cub}}$ ,  $\sqrt{2}a_{\text{cub}}$ ), and is ranked 27th among the lowest- $R_{wp}$  candidates. All lower- $R_{wp}$  candidates contain the same active modes as this candidate, but also have additional  $\Delta$ -,  $\Sigma$ -, and  $W$ -point modes which are not needed to fit the key structural features encoded in the current diffraction data. Performing a Hamilton-type test using either  $R_{wp}$  or  $R(F^2)$  agreement indicators, even with an overly optimistic estimate of the true number of observables in the powder data, supports candidate #152 as the best solution.<sup>57</sup>

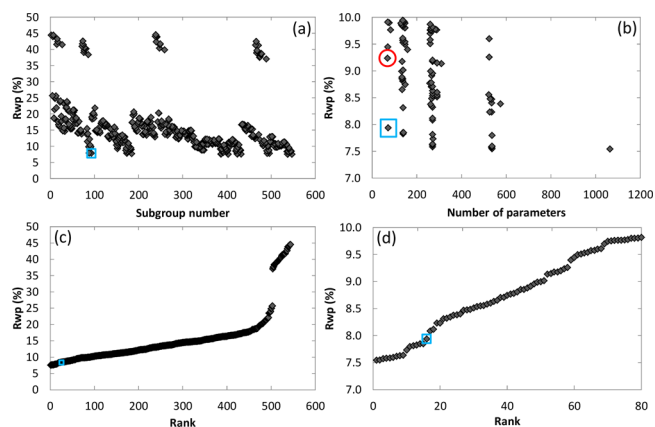


**Figure 5.** Final  $R_{wp}$  values from refinements of the 547 candidate models for  $\alpha$ - $\text{Bi}_2\text{Sn}_2\text{O}_7$  against  $\sim 293$  K X-ray and neutron diffraction data. Individual panels are  $\alpha$ -phase equivalents to those in Figure 4. Candidate #152 (our best  $\beta$ -structure model) is marked with a red circle, and candidate #88 (our best  $\alpha$ -structure model) is marked with a blue square.

Similar conclusions can be drawn from the equivalent plots for the  $\alpha$ -phase shown in Figure 5. In Figure 5a,c, we see that candidate models fall into two broad categories with  $R_{wp} \lesssim 25\%$  and  $R_{wp} \gtrsim 37\%$ . This break is associated with a single essential  $\Gamma_3^+$  mode. Focusing on the best candidates (Figure 5d), the drop in  $R_{wp}$  value at the 16th-ranked candidate (blue square) is associated with the switching on of an essential  $\Gamma_2^+$  mode, at which point all active modes are included. Lower- $R_{wp}$  candidates have additional  $\Delta$ -,  $\Sigma$ -,  $X$ -, and  $W$ -point modes, which are not needed to adequately fit the data. The plot of  $R_{wp}$  against the number of structural parameters (Figure 5b) therefore shows that #88 ( $Cc$ ,  $R_{wp} = 7.94\%$ , 16th in rank, 72 parameters, marked with a blue square) is the standout candidate; its monoclinic cell parameters are  $a = 13.15 \text{ \AA}$ ,  $b = 7.54 \text{ \AA}$ ,  $c = 13.14 \text{ \AA}$ ,  $\beta = 110^\circ$  ( $\sqrt{3/2}a_{\text{cub}}$ ,  $a_{\text{cub}}/\sqrt{2}$ ,  $\sqrt{3/2}a_{\text{cub}}$ ) and it gives an excellent fit to the data. The second-best candidate is one of #173 and #174 (see Table S2), which both have  $Pc$  symmetry on the same lattice and approximately twice the number of refineable parameters as #88. A Hamilton test again confirms #88 as the best model for the  $\alpha$ -phase, and examination of the Rietveld profiles shows that all the extra reflections predicted by larger-cell low- $R_{wp}$  models have zero observed intensity.

**Structural Discussion.** Our exhaustive subgroup search suggests relatively simple models for both  $\beta$ - and  $\alpha$ - $\text{Bi}_2\text{Sn}_2\text{O}_7$ . Full Rietveld refinements for each give excellent fits to the experimental data (Figure 6). Refinement details, important bond distances, and bond valence sums are included in Tables 2 and 3. For the  $\beta$ -phase we highlight the small splitting of the (4 8 0) and (0 8 8) reflections at  $d \approx 1.55 \text{ \AA}$ , characteristic of the small deviation from a metrically cubic cell ( $\Delta d/d < 5 \times 10^{-4}$ ; inset to Figure 6a). This splitting is a good differentiator among the various intermediate lattices in the tree. We also see excellent agreement with weak peaks at the  $X$ -point (Figure S3), which are visible in the diffraction pattern of  $\beta$ - but not  $\alpha$ - $\text{Bi}_2\text{Sn}_2\text{O}_7$ .

We can gain insight into the important structural distortions of the  $\alpha$ - and  $\beta$ -phases from the refined symmetry-mode amplitudes. Direct comparison of the two structures is complicated by the absence of a group–subgroup relationship between them. It is, however, possible to compare them by

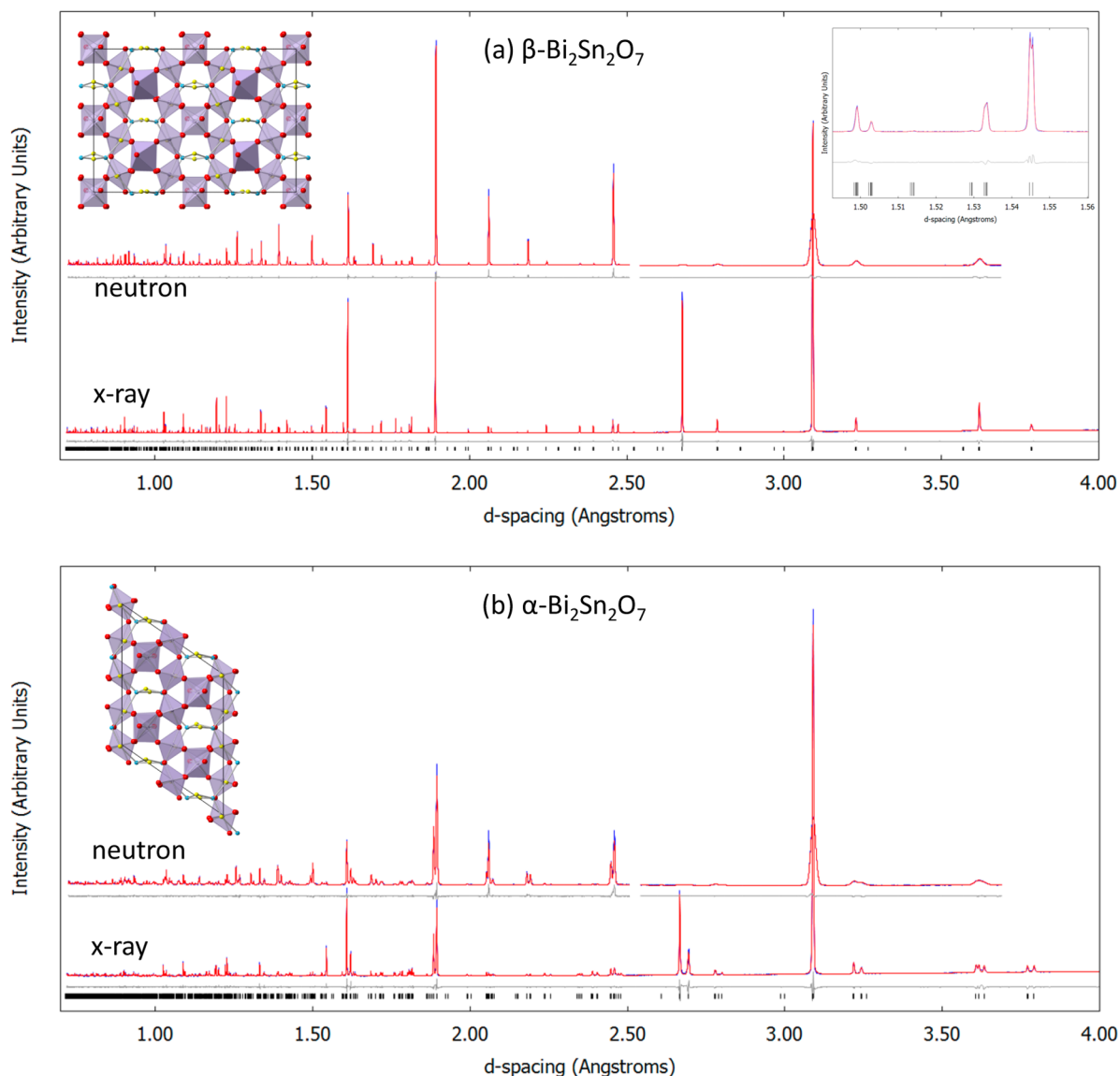


**Figure 6.** Final Rietveld fits for (a)  $\beta$ - $\text{Bi}_2\text{Sn}_2\text{O}_7$  and (b)  $\alpha$ - $\text{Bi}_2\text{Sn}_2\text{O}_7$  models. Neutron data have been scaled and offset vertically for plotting. Neutron data for  $d > 2.5 \text{ \AA}$  are from the lower resolution  $90^\circ$  data bank. Inset to (a) shows X-ray fit in the region of the (4 8 0) and (0 8 8) reflections at  $d \approx 1.55 \text{ \AA}$ , which would be unsplit for a metrically cubic cell. Structure insets are views down  $[0 1 0]$ , key as in Figure 1.

transforming each to their highest common subgroup, candidate #174 (see SI for details). #174 (space group  $Pc$ ) is a subgroup of index 2 for both models; it has the same lattice as  $\beta$ , and the same point group as  $\alpha$ . Figure 7 compares non-zero-mode amplitudes in this common subgroup. Note that some modes get split in two in the subgroup, e.g., the  $L_2^+(a,0,-a,0)$  mode of  $\beta$  (#152) splits into the separate  $a$  and  $b$  branches of  $L_2^+(a,b,0,0)$  in #174 with  $b = -a$ .

The 534-parameter  $\alpha_{\text{old}}\text{-Bi}_2\text{Sn}_2\text{O}_7$  model (candidate #537, lattice subgroup #547) also proves to be a common subgroup of the new  $\alpha$  (#88) and  $\beta$  (#152) models, though not the highest-symmetry one. This explains why it has sufficient freedom to fit both the  $\alpha$ - and  $\beta$ -phase data so well across the phase transition at 390 K, despite the structural differences between the two phases ( $R_{\text{wp}} = 7.580$  and rank = 4 for  $\alpha$ ;  $R_{\text{wp}} = 4.180$  and rank = 5 for  $\beta$ ).

We can see from Figure 7 that similar modes are important in each structure: large  $\Gamma_5^-$  (shaded pink) and  $L_2^+$  (yellow) Bi-modes and smaller  $\Gamma_4^-$  (green) modes on all atoms. It is worth

noting that for both structures the specific superposition of the appropriate  $\Gamma_5^-$  and  $L_2^+$  order parameters is primary (i.e., solely responsible for breaking the symmetry of the  $\gamma$  parent). We can also see that the magnitudes of modes associated with the  $\text{Bi}_2\text{O}'$  framework are much larger than those associated with  $\text{SnO}_6$ . This is reflected in the mean atomic displacements from ideal positions for the different atom types in the  $\alpha$  ( $\beta$ )-structure of Bi 0.381  $\text{\AA}$  (0.355  $\text{\AA}$ ), Sn 0.059  $\text{\AA}$  (0.041  $\text{\AA}$ ), O 0.148  $\text{\AA}$  (0.118  $\text{\AA}$ ), and O' 0.253  $\text{\AA}$  (0.140  $\text{\AA}$ ). The Bi displacement is similar to that found in PDF studies of disordered  $\text{Bi}_2\text{Ti}_2\text{O}_7$ .<sup>21</sup>

The effect of the large  $\Gamma_5^-$  and  $L_2^+$  modes is to cause rotations of the  $\text{Bi}_4\text{O}'$  tetrahedra with minimal internal distortion of their bond distances and angles (Figure 8). In the undistorted parent structure the  $\text{Bi}_4\text{O}'$  tetrahedra are close to regular: Bi–O' distances are 2.315–2.317  $\text{\AA}$  and angles 108.9–109.8° (the ranges presented from here on encompass all crystallographically distinct coordination environments). With both  $\Gamma_5^-$  and  $L_2^+$  modes active, these ranges do not change greatly: 2.33–2.36  $\text{\AA}$ /108.7–110.6° for the  $\alpha$  structure and 2.32–2.36

**Table 2. Structural Parameters from Rietveld Refinement of Combined XRPD and NPD Data at ~295 K (left) and 470 K (right)**

$\alpha$ -Bi <sub>2</sub> Sn <sub>2</sub> O <sub>7</sub> , space group <i>Cc</i>					$\beta$ -Bi <sub>2</sub> Sn <sub>2</sub> O <sub>7</sub> , space group <i>Aba2</i>				
atom	<i>x</i>	<i>y</i>	<i>z</i>	<i>B</i> /Å <sup>2</sup>	atom	<i>x</i>	<i>y</i>	<i>z</i>	<i>B</i> /Å <sup>2</sup>
Bi-1	0.2369(2)	0.2673(3)	0.01442(17)	0.858(11)	Bi-1	0.7097(2)	0.11466(9)	0.11170(13)	1.421(5)
Bi-2	0.2743(2)	0.2245(3)	0.51155(17)	0.858(11)	Bi-2	0.2894(2)	0.36431(9)	0.36150(13)	1.421(5)
Bi-3	-0.0174(2)	-0.0446(3)	-0.02055(19)	0.858(11)	Bi-3	0.0255(2)	0.23624(6)	0.00458(12)	1.421(5)
Bi-4	0.0306(2)	0.0038(3)	0.75004(19)	0.858(11)	Bi-4	0	0	0.23244(14)	1.421(5)
Sn-1	0.7501(4)	0.2474(6)	0.7500(3)	0.485(10)	Bi-5	0	0	0.76936(14)	1.421(5)
Sn-2	0.7436(4)	0.2512(6)	0.2420(3)	0.485(10)	Sn-1	0.7486(4)	0.37511(8)	0.12465(12)	0.602(5)
Sn-3	0.4972(3)	0.0010(6)	0.7465(3)	0.485(10)	Sn-2	0.2473(4)	0.62452(8)	0.37231(12)	0.602(5)
Sn-4	0.4960(3)	0.0005(4)	0.4943(3)	0.485(10)	Sn-3	0	0	-0.0003(2)	0.602(5)
O1-1	0.6192(4)	0.2064(6)	0.7820(4)	0.738(9)	Sn-4	0	0	0.4948(2)	0.602(5)
O1-2	0.6158(4)	0.2065(6)	0.2751(4)	0.738(9)	Sn-5	0.5021(3)	0.24797(12)	0.24736(15)	0.602(5)
O1-3	0.1297(4)	0.3117(6)	0.0862(4)	0.738(9)	O1-1	0.4473(9)	0.6872(3)	0.3492(4)	1.050(8)
O1-4	0.1165(4)	0.2853(6)	0.5814(4)	0.738(9)	O1-2	0.4537(9)	0.1888(3)	0.3564(4)	1.050(8)
O1-5	0.8200(5)	-0.0005(6)	0.7907(4)	0.738(9)	O1-3	-0.0488(9)	0.4350(3)	0.0967(4)	1.050(8)
O1-6	0.4222(5)	-0.0126(6)	0.0849(4)	0.738(9)	O1-4	-0.0536(9)	0.9394(3)	0.1065(4)	1.050(8)
O1-7	0.8632(4)	0.3052(6)	0.9113(4)	0.738(9)	O1-5	0.0635(9)	0.1918(3)	0.1471(4)	1.050(8)
O1-8	0.8768(4)	0.2983(6)	0.4044(4)	0.738(9)	O1-6	0.0400(9)	0.6828(3)	0.1520(4)	1.050(8)
O1-9	0.3596(4)	0.1979(6)	0.1981(4)	0.738(9)	O1-7	0.5406(9)	0.4352(3)	0.3998(4)	1.050(8)
O1-10	0.3563(4)	0.1915(6)	0.6966(4)	0.738(9)	O1-8	0.5552(9)	0.9410(3)	0.3983(4)	1.050(8)
O1-11	0.1728(5)	0.0011(6)	0.2204(4)	0.738(9)	O1-9	0.7208(7)	0.3412(2)	0.0008(4)	1.050(8)
O1-12	0.5666(5)	-0.0221(6)	0.9057(4)	0.738(9)	O1-10	0.2543(7)	0.5868(2)	0.2473(4)	1.050(8)
O2-1	0.1443(6)	0.0057(6)	0.9446(4)	1.06(3)	O1-11	0.7490(9)	0.0360(3)	0.0126(5)	1.050(8)
O2-2	0.9004(6)	-0.0047(6)	0.0692(4)	1.06(3)	O1-12	0.2541(8)	0.2866(3)	0.2608(5)	1.050(8)
					O2-1	0.7482(14)	0.1902(3)	-0.0085(5)	2.37(4)
					O2-2	0.2472(11)	0.4394(3)	0.2414(5)	2.37(4)

$a = 13.15493(6)$  Å,  $b = 7.54118(4)$  Å,  $c = 15.07672(7)$  Å,  $\beta = 125.0120(3)^\circ$

$R_{wp}$  ( $R_{Bragg}$ ): PND(bs/90°), 5.56% (3.27%)/2.10% (1.18%)

XRPD: 5.96% (2.15%); overall,  $R_{wp} = 5.65\%$ ,  $R_p = 3.84\%$ , GOF = 1.73

$a = 7.571833(8)$  Å,  $b = 21.41262(2)$  Å,  $c = 15.132459(14)$  Å

$R_{wp}$  ( $R_{Bragg}$ ): PND(bs/90°), 4.07% (2.97%)/2.94% (1.35%)

XRPD: 4.93% (3.22%); overall,  $R_{wp} = 4.55\%$ ,  $R_p = 3.05\%$ , GOF = 1.76

**Table 3. Bond Distances and Bond Valence Sums in  $\beta$ - and  $\alpha$ -Bi<sub>2</sub>Sn<sub>2</sub>O<sub>7</sub>**

atom	O distances/Å				O' distances/Å				BVS
	$\beta$ -Bi <sub>2</sub> Sn <sub>2</sub> O <sub>7</sub>								
Bi1	2.239(7)	2.275(7)	2.465(7)	2.850(7)	3.111(7)	3.192(7)	2.296(8)	2.452(8)	2.83
Bi2	2.272(7)	2.287(7)	2.502(7)	2.786(7)	3.133(7)	3.142(7)	2.305(8)	2.447(8)	2.74
Bi3	2.222(5)	2.375(7)	2.466(7)	2.868(7)	2.927(7)	3.221(7)	2.315(9)	2.328(10)	2.87
Bi4	2.342(7)	2.342(7)	2.639(5)	2.639(5)	2.904(7)	2.904(7)	2.317(8)	2.317(8)	2.77
Bi5	2.361(7)	2.361(7)	2.696(5)	2.696(5)	2.983(7)	2.983(7)	2.317(8)	2.317(8)	2.61
Sn1	2.021(7)	2.027(7)	2.033(7)	2.037(7)	2.044(7)	2.066(7)			4.19
Sn2	2.053(7)	2.058(7)	2.060(7)	2.067(7)	2.088(7)	2.095(7)			3.84
Sn3	2.030(7)	2.030(7)	2.060(6)	2.060(6)	2.112(7)	2.112(7)			3.89
Sn4	2.020(7)	2.020(7)	2.055(6)	2.055(6)	2.110(7)	2.110(7)			3.95
Sn5	2.033(7)	2.044(7)	2.057(7)	2.062(7)	2.109(7)	2.113(7)			3.86
	$\alpha$ -Bi <sub>2</sub> Sn <sub>2</sub> O <sub>7</sub>								
Bi1	2.241(5)	2.328(5)	2.453(5)	2.925(5)	3.000(5)	3.145(5)	2.239(5)	2.495(6)	2.82
Bi2	2.256(5)	2.357(5)	2.393(5)	2.853(5)	2.883(5)	3.170(5)	2.230(6)	2.514(6)	2.87
Bi3	2.252(5)	2.378(5)	2.408(5)	2.937(5)	3.025(5)	3.159(5)	2.184(6)	2.496(6)	2.87
Bi4	2.158(5)	2.384(5)	2.444(5)	2.952(5)	3.056(5)	3.162(5)	2.237(6)	2.410(6)	2.99
Sn1	2.018(6)	2.038(6)	2.042(6)	2.061(6)	2.076(6)	2.078(6)			4.04
Sn2	2.005(6)	2.022(6)	2.037(6)	2.044(6)	2.066(6)	2.068(6)			4.17
Sn3	2.027(6)	2.039(6)	2.068(6)	2.073(6)	2.113(6)	2.131(6)			3.81
Sn4	2.025(6)	2.046(6)	2.055(6)	2.063(6)	2.082(6)	2.117(6)			3.91

Å/108.5–110.5° for the  $\beta$  structure. This suggests a view of both phase transitions similar to that for  $\beta$ - to  $\alpha$ -cristobalite, where  $X_4$  modes describe the coupled rotations of rigid SiO<sub>4/2</sub> tetrahedra on changing from  $Fd\bar{3}m$  to  $P4_12_12$ .<sup>27,58</sup>

The  $\Gamma_5^-$  and  $L_2^+$  modes give rise to tetrahedral rotations around different axes. Both the *Aba2*  $\beta$ -phase and *Cc*  $\alpha$ -phase subgroup symmetries adopt the specific order parameter direction (OPD)  $\Gamma_5^-(0,a,a)$ , which corresponds to a coupled



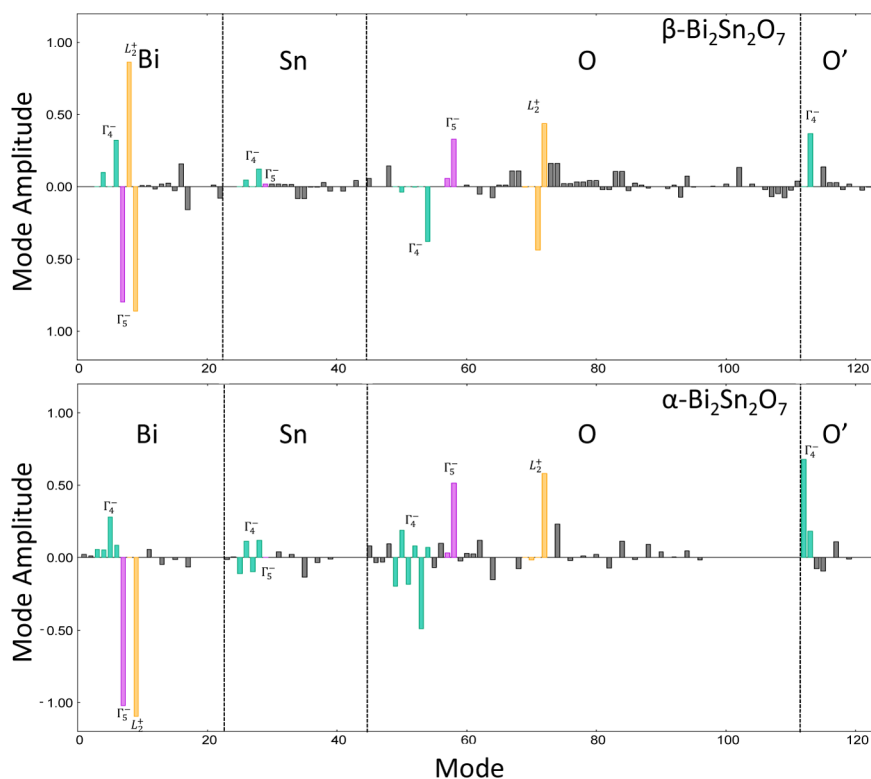


**Figure 7.** Mode amplitudes in (top)  $\beta$ - and (bottom)  $\alpha$ - $\text{Bi}_2\text{Sn}_2\text{O}_7$  when reduced to a common subgroup setting ( $Pc$ , #174) with the appropriate domain and origin choice. Irreps not found in a structure are shown with zero amplitude. Irreps are plotted in order of parent atom type and color coded by irrep ( $\Gamma_4^-$ , green;  $\Gamma_5^-$ , pink;  $L_2^+$ , yellow; others, gray). Absolute-mode amplitude sums  $\alpha$  ( $\beta$ ):  $\Sigma_{\text{Bi}} = 2.81 \text{ \AA}$  (3.46  $\text{\AA}$ ),  $\Sigma_{\text{Sn}} = 0.70 \text{ \AA}$  (0.56  $\text{\AA}$ ),  $\Sigma_{\text{O1}} = 3.87 \text{ \AA}$  (3.75  $\text{\AA}$ ),  $\Sigma_{\text{O}'} = 1.15 \text{ \AA}$  (0.63  $\text{\AA}$ ).

rotation of  $\text{Bi}_4\text{O}'$  tetrahedra around an axis parallel to  $\langle 1\ 1\ 0 \rangle$  of the parent structure as shown in the top row of Figure 8. This causes Bi atoms to displace in the plane of their puckered hexagonal O coordination environment, moving toward a specific hexagon edge (the  $96h$  site of the parent structure). The  $\Gamma_5^-$  distortion corresponds to a  $7.7^\circ$  rotation of tetrahedra around the  $b$ -axis of the  $\alpha$ -cell, and  $6.0^\circ$  around the  $a$ -axis of the  $\beta$ -cell.

The effect of the four-mode  $L_2^+(a,b,c,d)$  order parameter is more complex, but the different OPDs it adopts are what distinguish the  $\alpha$ - and  $\beta$ -structures. The difference is easy to visualize in the common subgroup #174 where the  $\alpha$ -structure adopts  $L_2^+(0,a,0,0)$  and the  $\beta$ -structure adopts  $L_2^+(a,b,0,0)$  with  $a = -b$ . These  $L_2^+$  differences are also seen clearly in the bar chart of Figure 7, where the  $a$  and  $b$  branches of the  $L_2^+$  OPD have two modes of equal amplitude but opposite sign for the  $\beta$ -phase and only one mode for the  $\alpha$ -phase. The  $L_2^+(0,a,0,0)$  mode of  $\alpha$ -phase corresponds to an  $8.2^\circ$  rotation of pairs of  $\text{Bi}_3\text{O}'\text{BiO}'\text{Bi}_3$  tetrahedra around the parent  $[1\ 1\ 1]$  axis with the  $\text{Bi}-\text{O}'-\text{Bi}$  bond angle on the  $[1\ 1\ 1]$  axis unchanged, but other  $\text{Bi}-\text{O}'-\text{Bi}$  angles changing as shown in the lowest panel of Figure 8. The  $L_2^+(a,0,0,0)$  mode, which produces an equivalent rotation around  $[1\ -1\ 1]$  axis, contributes to  $\beta$  but not  $\alpha$  (middle row of Figure 8), thus rotating one  $\text{Bi}_4\text{O}'$  tetrahedron by  $10.5^\circ$  around the  $c$ -axis and the other by  $7.5^\circ$  around the  $a$ -axis of the  $\beta$ -phase cell. The most significant difference between the two structures is the simpler  $\langle 1\ 1\ 1 \rangle$  rotation of the  $\alpha$ -phase.

The overall effect of the tilts on the local Bi coordination is shown in Figure 9. In the  $\beta$ -structure, the roughly equal amplitude  $\Gamma_5^-$  and  $L_2^+$  modes move four of the five Bi sites toward a hexagon edge and leave one (Bi4) unshifted. The

result is that each Bi has two short (2.22–2.45  $\text{\AA}$ ) and four longer (2.47–3.19  $\text{\AA}$ ) bonds to O. The  $\beta$ -structure therefore has Bi environments similar to those proposed for disordered cubic  $\text{Bi}_2\text{Ti}_2\text{O}_7$  phases. In the  $\alpha$ -structure the combined  $\Gamma_5^-$  and  $L_2^+$  modes move Bi principally toward a hexagon vertex (only Bi4 moves precisely along the parent  $\text{Bi}-\text{O}$  vector), leading to three short (2.10–2.45  $\text{\AA}$ ) and three longer  $\text{Bi}-\text{O}$  bonds (2.85–3.17  $\text{\AA}$ ). The difference in the number of short  $\text{Bi}-\text{O}$  bonds (two for  $\beta$  and three for  $\alpha$ ) is accompanied by significantly different  $\text{Bi}_2\text{O}'$  framework distortions. In the  $\beta$ -structure,  $\text{Bi}-\text{O}'$  axial bonds in each Bi hexagonal bipyramid are reasonably symmetric (eight are  $2.31 \pm 0.01 \text{ \AA}$ ; two are 2.45  $\text{\AA}$ ). In the  $\alpha$ -structure, each Bi has one short (2.16–2.24  $\text{\AA}$ )  $\text{Bi}-\text{O}'$  bond and one longer  $\text{Bi}-\text{O}'$  (2.41–2.51  $\text{\AA}$ ) bond. Overall, in the  $\alpha$ -structure the four Bi coordination environments are very similar, with five short bonds and three longer. In the  $\beta$ -structure the Bi environments are less uniform. Three are similar to  $\alpha$  with five short and three longer bonds, whereas two (Bi4 and Bi5) lie on the 2-fold axis and have four short ( $\sim 2.3 \text{ \AA}$ ), two intermediate ( $\sim 2.7 \text{ \AA}$ ), and two long ( $\sim 2.9 \text{ \AA}$ ) bonds.

## CONCLUSIONS

Symmetry modes provide a natural basis for both solving and describing structures that arise from phase transitions in complex functional materials. Here we demonstrate an automated and exhaustive symmetry-mode analysis of all possible superstructures derived from a parent phase, up to a maximum cell size that accommodates experimentally observed superlattice peaks and any other relevant evidence. The method provides a comprehensive, systematic, and straightforward comparison of different candidate models.

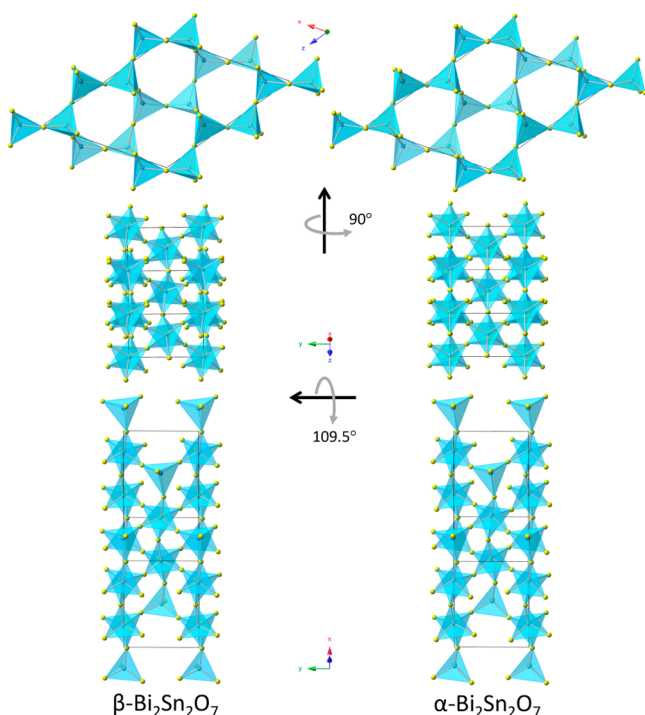


**Figure 8.** Views of  $\text{Bi}_2\text{O}'$  framework tetrahedral rotations dominated by  $\Gamma_5^-$  and  $L_2^+$  modes in  $\alpha$ - and  $\beta$ - $\text{Bi}_2\text{Sn}_2\text{O}_7$  shown in the common subgroup setting of candidate #174. Top view is down  $[0\ 1\ 0]$ , middle view down  $[-2\ 0\ 1]$ , lower view down  $[-2\ 0\ 3]$ ; these correspond to  $[-1\ 0\ 1]$ ,  $[1\ -1\ 1]$ , and  $[1\ 1\ 1]$  of parent structure. Bi and O' atoms are shown in yellow and blue, respectively. An animated view and equivalent views of  $\gamma$ - $\text{Bi}_2\text{Sn}_2\text{O}_7$  are available (Figure S6).

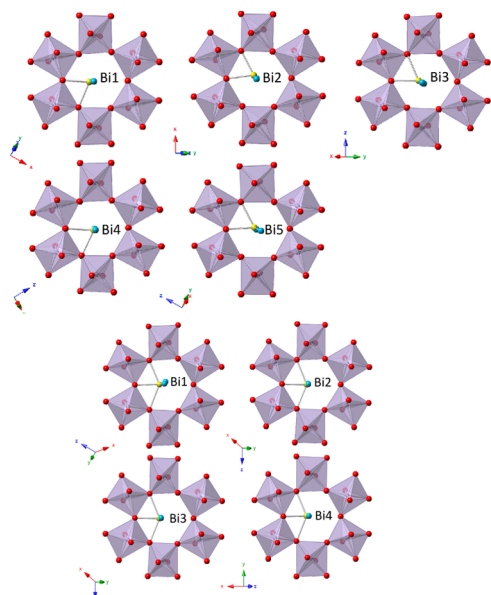


**Figure 9.** Bi coordination environments in (upper panel)  $\beta$ - and (lower panel)  $\alpha$ - $\text{Bi}_2\text{Sn}_2\text{O}_7$ . Bi and O' atoms are shown in yellow and blue, respectively, while  $\text{SnO}_6$  octahedra are gray.

We then demonstrate this approach in a detailed study of  $\text{Bi}_2\text{Sn}_2\text{O}_7$ , where there has been significant controversy over the structures in its phase diagram. We describe how to identify the sublattice of each observed phase directly from experimental observations, which leads to a relatively short list of 62 candidate structures to explore. We also show how to explore

all 547 candidate structures that are consistent with previously reported models. Despite the subtlety and complexity of the distortions involved, we obtained unambiguous solutions to both the  $\alpha$ - and  $\beta$ -phase structures.

We describe the first reliable structure for  $\beta$ - $\text{Bi}_2\text{Sn}_2\text{O}_7$ , with orthorhombic space group  $Aba2$ , and an  $\alpha$ - $\text{Bi}_2\text{Sn}_2\text{O}_7$  structure far simpler than previously reported, with monoclinic space group  $Cc$ . Relative to all other superstructural models, our solutions unambiguously optimize fits to the combined X-ray and neutron powder diffraction data sets with a minimum number of structural parameters.

The symmetry-mode parameterizations of the  $\alpha$ - and  $\beta$ - $\text{Bi}_2\text{Sn}_2\text{O}_7$  structures further illuminate their phase transitions in terms of rotations of the cristobalite-like  $\text{Bi}_2\text{O}'$  framework, which displace Bi toward an edge of the O6 coordination hexagon in  $\beta$  and toward a vertex in  $\alpha$ . These different distortions allow Bi to adopt the asymmetric coordination environment typical of a lone pair cation. Our exhaustive analysis leads us to believe that we now have definitive models for the known phases of this fascinating material.

The present combination of symmetry-mode analysis and exhaustive subgroup searching significantly expands the scope of structure determination in materials that exhibit complex symmetry-lowering phase transitions. These include fuel cells,<sup>59</sup> Li-ion batteries<sup>60</sup> and other vacancy or cation-ordered materials,<sup>61</sup> metallic alloys, negative-thermal expansion materials,<sup>62,63</sup> ferroelectrics,<sup>64</sup> piezoelectrics,<sup>65</sup> and other multiferroic systems,<sup>66,67</sup> superconductors,<sup>68</sup> and correlated-electron systems with competing lattice, charge, orbital, and magnetic degrees of freedom.<sup>69–71</sup> Simple extensions of the present methods would include magnetic phase transitions, occupational orderings, whole-molecule reorientations, thermal vibrations, and polyhedral tilts.

## ■ ASSOCIATED CONTENT

### § Supporting Information

The Supporting Information is available free of charge on the ACS Publications website at DOI: 10.1021/jacs.6b04947.

Graph of  $R_{\text{wp}}$  for three repeat exhaustive trials of all candidate models against  $\alpha$ - and  $\beta$ -phase data; multiphase Rietveld fit of  $\alpha$ - $\text{Bi}_2\text{Sn}_2\text{O}_7$  X-ray data to show strain broadening; Rietveld fit to  $\alpha$ - and  $\beta$ -phase X-ray data using best candidate models, showing weak X-point distortions of the  $\beta$ -phase; histogram showing magnitude of displacive modes in  $\alpha_{\text{old}}$ - $\text{Bi}_2\text{Sn}_2\text{O}_7$ ; Rietveld fit of  $\alpha$ - $\text{Bi}_2\text{Sn}_2\text{O}_7$  X-ray data using  $Cc$  and  $Pc$  candidates; version of Figure 8 with parent  $\gamma$ -phase included; discussion of transformation of  $\alpha$ - and  $\beta$ -structures to their highest common subgroup; table listing all 547 candidate models; table showing the 30 lowest  $R_{\text{wp}}$  candidates for the  $\alpha$ - and  $\beta$ -phases (PDF)

Crystallographic information file of  $\gamma$  parent structure (CIF)

Crystallographic information file of  $\alpha$ -structure (CIF)

Crystallographic information file of  $\beta$ -structure (CIF)

Crystallographic information file of  $\alpha$ -structure in subgroup 174 setting (CIF)

Crystallographic information file of  $\beta$ -structure in subgroup 174 setting (CIF)

ISODISTORT distortion file for the structure in subgroup 174 setting relative to the parent structure: alpha\_st174-gamma\_distortion (TXT)

Equivalent ISODISTORT distortion file for : beta\_st174\_domain17-gamma\_distortion (TXT)  
ISODISTORT distortion file for animated view of Figure 8 (left): bi2o\_gamma\_alpha\_st174\_bi4o\_distortion (TXT)  
ISODISTORT distortion file for animated view of Figure 8 (right): bi2o\_gamma\_beta\_st174\_domain17\_distortion (TXT)

## AUTHOR INFORMATION

### Corresponding Author

\*john.evans@durham.ac.uk

### Present Address

J.L.P.: School of Chemistry, University of St Andrews, North Haugh, St Andrews, Fife, Scotland, United Kingdom.

### Notes

The authors declare no competing financial interest.

## ACKNOWLEDGMENTS

B.J.C. would like to acknowledge the US-UK Fulbright commission for a research fellowship and the University of Durham for hosting his research leave. J.W.L. would like to thank the EPSRC for a Ph.D. scholarship. We thank Chris Howard for useful discussions on Bi<sub>2</sub>Sn<sub>2</sub>O<sub>7</sub>. We thank ISIS and Diamond for access to neutron and synchrotron facilities.

## REFERENCES

- (1) Setter, N.; Damjanovic, D.; Eng, L.; Fox, G.; Gevorgian, S.; Hong, S.; Kingon, A.; Kohlstedt, H.; Park, N.; Stephenson, G. B.; et al. *J. Appl. Phys.* **2006**, *100*, 051606.
- (2) Eerenstein, W.; Mathur, N. D.; Scott, J. F. *Nature* **2006**, *442*, 759.
- (3) Salje, E. *Ferroelectrics* **1990**, *104*, 111.
- (4) Hoshi, H.; Nakamura, N.; Maruyama, Y.; Nakagawa, T.; Suzuki, S.; Shiromaru, H.; Achiba, Y. *Jpn. J. Appl. Phys., Part 2* **1991**, *30*, L1397.
- (5) Evans, J. S. O. *J. Chem. Soc., Dalton Trans.* **1999**, 3317.
- (6) Imada, M.; Fujimori, A.; Tokura, Y. *Rev. Mod. Phys.* **1998**, *70*, 1039.
- (7) Lottermoser, T.; Lonkai, T.; Amann, U.; Hohlwein, D.; Ihringer, J.; Fiebig, M. *Nature* **2004**, *430*, 541.
- (8) Müller, U. *Symmetry relationships between crystal structures: applications of crystallographic group theory in crystal chemistry*; OUP: Oxford, 2013.
- (9) Cook, W. R., Jr; Jaffe, H. *Phys. Rev.* **1952**, *88*, 1426.
- (10) Buixaderas, E.; Kamba, S.; Petzelt, J. *Ferroelectrics* **2004**, *308*, 131.
- (11) Hanawa, M.; Muraoka, Y.; Tayama, T.; Sakakibara, T.; Yamaura, J.; Hiroi, Z. *Phys. Rev. Lett.* **2001**, *87*, 187001.
- (12) Van Dijk, M. P.; De Vries, K. J.; Burggraaf, A. J. *Solid State Ionics* **1983**, *9*, 913.
- (13) Subramanian, M. A.; Toby, B. H.; Ramirez, A. P.; Marshall, W. J.; Sleight, A. W.; Kwei, G. *Science* **1996**, *273*, 81.
- (14) Coles, G. S. V.; Bond, S. E.; Williams, G. J. *Mater. Chem.* **1994**, *4*, 23.
- (15) Sleight, A. W.; Gillson, J. L. *Mater. Res. Bull.* **1971**, *6*, 781.
- (16) Ramirez, A. P.; Hayashi, A.; Cava, R. J.; Siddharthan, R.; Shastri, B. S. *Nature* **1999**, *399*, 333.
- (17) Laverov, N. P.; Yuditsev, S. V.; Livshits, T. S.; Stefanovsky, S. V.; Lukinykh, A. N.; Ewing, R. C. *Geochem. Int.* **2010**, *48*, 1.
- (18) Merka, O.; Bahnmann, D. W.; Wark, M. *Catal. Today* **2014**, *225*, 102.
- (19) Sleight, A. W. *Inorg. Chem.* **1968**, *7*, 1704.
- (20) Radosavljevic, I.; Evans, J. S. O.; Sleight, A. W. *J. Solid State Chem.* **1998**, *136*, 63.
- (21) Shoemaker, D. P.; Seshadri, R.; Hector, A. L.; Llobet, A.; Proffen, T.; Fennie, C. J. *Phys. Rev. B: Condens. Matter Mater. Phys.* **2010**, *81*, 144113.
- (22) Shoemaker, D. P.; Seshadri, R.; Tachibana, M.; Hector, A. L. *Phys. Rev. B: Condens. Matter Mater. Phys.* **2011**, *84*, 064117.
- (23) Seshadri, R. *Solid State Sci.* **2006**, *8*, 259.
- (24) Harris, M. J.; Bramwell, S. T.; McMorrow, D. F.; Zeiske, T.; Godfrey, K. W. *Phys. Rev. Lett.* **1997**, *79*, 2554.
- (25) Avdeev, M.; Haas, M.; Jorgensen, J.; Cava, R. J. *Solid State Chem.* **2002**, *169*, 24.
- (26) Facer, G. R.; Elcombe, M. M.; Kennedy, B. J. *Aust. J. Chem.* **1993**, *46*, 1897.
- (27) Goodwin, A. L.; Withers, R. L.; Nguyen, H. B. *J. Phys.: Condens. Matter* **2007**, *19*, 335216.
- (28) Wang, X.; Wang, H.; Yao, X. *J. Am. Ceram. Soc.* **1997**, *80*, 2745.
- (29) Liu, Y.; Withers, R. L.; Welberry, T. R.; Wang, H.; Du, H. *J. Solid State Chem.* **2006**, *179*, 2141.
- (30) Krayzman, V.; Levin, I.; Woicik, J. C. *Chem. Mater.* **2007**, *19*, 932.
- (31) Ren, W.; Trolier-McKinstry, S.; Randall, C. A.; Shrout, T. R. *J. Appl. Phys.* **2001**, *89*, 767.
- (32) Moens, L.; Ruiz, P.; Delmon, B.; Devillers, M. *Catal. Lett.* **1997**, *46*, 93.
- (33) Moens, L.; Ruiz, P.; Delmon, B.; Devillers, M. *Appl. Catal., A* **1998**, *171*, 131.
- (34) Moens, L.; Ruiz, P.; Delmon, B.; Devillers, M. *Appl. Catal., A* **1999**, *180*, 299.
- (35) Mims, C. A.; Jacobson, A. J.; Hall, R. B.; Lewandowski, J. T. *J. Catal.* **1995**, *153*, 197.
- (36) Tian, Q.; Zhuang, J.; Wang, J.; Xie, I.; Liu, P. *Appl. Catal., A* **2012**, *425*, 74.
- (37) Devi, G. S.; Manorama, S. V.; Rao, V. J. *J. Electrochem. Soc.* **1998**, *145*, 1039.
- (38) Devi, G. S.; Manorama, S. V.; Rao, V. J. *Sens. Actuators, B* **1999**, *56*, 98.
- (39) Malinovskaya, T. D.; Aparnev, A. I.; Egorov, Y. P.; Yukhin, Y. M. *Russ. J. Appl. Chem.* **2001**, *74*, 1864.
- (40) Roth, R. S. *J. Res. Natl. Bur. Stand* **1956**, *56*, 17.
- (41) Shannon, R. D.; Bierlein, J. D.; Gillson, J. L.; Jones, G. A.; Sleight, A. W. *J. Phys. Chem. Solids* **1980**, *41*, 117.
- (42) Jones, R. H.; Knight, K. S. *J. Chem. Soc., Dalton Trans.* **1997**, 2551.
- (43) Walsh, A.; Watson, G. W. *Chem. Mater.* **2007**, *19*, 5158.
- (44) Kennedy, B. J.; Ismunandar; Elcombe, M. *Mater. Sci. Forum* **1998**, *278*, 762.
- (45) Evans, I. R.; Howard, J. A. K.; Evans, J. S. O. *J. Mater. Chem.* **2003**, *13*, 2098.
- (46) Payne, J. L. Doctoral Thesis, Durham University, Durham, UK, 2010.
- (47) Salamat, A.; Hector, A. L.; McMillan, P. F.; Ritter, C. *Inorg. Chem.* **2011**, *50*, 11905.
- (48) Campbell, B. J.; Stokes, H. T.; Tanner, D. E.; Hatch, D. M. *J. Appl. Crystallogr.* **2006**, *39*, 607.
- (49) Aroyo, M. I.; Perez-Mato, J. M.; Orobengoa, D.; Tasci, E.; De La Flor, G.; Kirov, A.; et al. *Acta Crystallogr., Sect. A: Found. Crystallogr.* **2011**, *43*, 183.
- (50) Aroyo, M. I.; Perez-Mato, J. M.; Capillas, C.; Kroumova, E.; Ivantchev, S.; Madariaga, G.; Kirov, A.; Wondratschek, H. *Z. Kristallogr. - Cryst. Mater.* **2006**, *221*, 15.
- (51) Aroyo, M. I.; Kirov, A.; Capillas, C.; Perez-Mato, J. M.; Wondratschek, H. *Acta Crystallogr., Sect. A: Found. Crystallogr.* **2006**, *62*, 115.
- (52) Coelho, A. A. *TOPAS Academic: General Profile and Structure Analysis Software for Powder Diffraction Data*; Bruker AXS: Karlsruhe, Germany, 2012.
- (53) Coelho, A. A.; Evans, J. S. O.; Evans, I. R.; Kern, A.; Parsons, S. *Powder Diffr.* **2011**, *26*, S22.
- (54) Stephens, P. W. *J. Appl. Crystallogr.* **1999**, *32*, 281.
- (55) Wells, S. A.; Sartbaeva, A. *Mol. Simul.* **2015**, *41*, 1409.

- (56) Wells, S. A.; Dove, M. T.; Tucker, M. G. *J. Phys.: Condens. Matter* **2002**, *14*, 4567.
- (57) Hamilton, W. C. *Acta Crystallogr.* **1965**, *18*, 502.
- (58) Hatch, D. M.; Ghose, S. *Phys. Chem. Miner.* **1991**, *17*, 554.
- (59) Pramana, S. S.; Baikie, T.; An, T.; Tucker, M. G.; Wu, J.; Schreyer, M. K.; Wei, F.; Bayliss, R. D.; Kloc, C. L.; White, T. J.; et al. *J. Am. Chem. Soc.* **2016**, *138*, 1273.
- (60) Ati, M.; Melot, B. C.; Chotard, J. N.; Rousse, G.; Reynaud, M.; Tarascon, J. M. *Electrochem. Commun.* **2011**, *13*, 1280.
- (61) Ainsworth, C. M.; Wang, C.-H.; Johnston, H. E.; McCabe, E. E.; Tucker, M. G.; Brand, H. E.; Evans, J. S. O. *Inorg. Chem.* **2015**, *54*, 7230.
- (62) Senn, M.; Bombardi, A.; Murray, C.; Vecchini, C.; Scherillo, A.; Luo, X.; Cheong, S. *Phys. Rev. Lett.* **2015**, *114*, 035701.
- (63) Senn, M. S.; Murray, C. A.; Luo, X.; Wang, L.; Huang, F.-T.; Cheong, S.-W.; Bombardi, A.; Ablitt, C.; Mostofi, A. A.; Bristowe, N. C. *J. Am. Chem. Soc.* **2016**, *138*, 5479.
- (64) Shi, Y.; Guo, Y.; Wang, X.; Princep, A. J.; Khalyavin, D.; Manuel, P.; Michiue, Y.; Sato, A.; Tsuda, K.; Yu, S.; et al. *Nat. Mater.* **2013**, *12*, 1024.
- (65) Dolgos, M. R.; Adem, U.; Manjon-Sanz, A.; Wan, X.; Comyn, T. P.; Stevenson, T.; Bennett, J.; Bell, A. J.; Tran, T. T.; Halasyamani, P. S.; Claridge, J. B.; Rosseinsky, M. J. *Angew. Chem., Int. Ed.* **2012**, *51*, 10770.
- (66) Kornev, I. A.; Bellaiche, L. *Phys. Rev. B: Condens. Matter Mater. Phys.* **2009**, *79*, 100105.
- (67) Dieguez, O.; Gonzalez-Vazquez, O. E.; Wojdel, J. C.; Iniguez, J. *Phys. Rev. B: Condens. Matter Mater. Phys.* **2011**, *83*, 094105.
- (68) Howard, C. J.; Carpenter, M. A. *Acta Crystallogr., Sect. B: Struct. Sci.* **2012**, *68*, 209.
- (69) Senn, M. S.; Wright, J. P.; Attfield, J. P. *Nature* **2012**, *481*, 173.
- (70) Ghosh, A.; Dey, K.; Chakraborty, M.; Majumdar, S.; Giri, S. *EPL* **2014**, *107*, 47012.
- (71) Svitlyk, V.; Chernyshov, D.; Bosak, A.; Pomjakushina, E.; Krzton-Maziopa, A.; Conder, K.; Pomjakushin, V.; Dmitriev, V.; Garbarino, G.; Mezouar, M. *Phys. Rev. B: Condens. Matter Mater. Phys.* **2014**, *89*, 144106.